Environmental Science Nano

Nanoparticle-templated polyamide membranes for improved biofouling resistance

Journal:	*Environmental Science: Nano*
Manuscript ID	EN-ART-11-2020-001101.R1
Article Type:	Paper

Environmental significance:

Fouling is a critical limitation for reverse osmosis systems that leads to an increase in the operational and environmental costs of desalination due to the extensive pre-treatments and chemical use involved in fouling management. Surface coatings have been widely used as a strategy to tailor the properties of desalination membranes and improve their fouling resistance; however, coatings tend to leach out or degrade over time. Here, we examine a membrane modification strategy that uses an interlayer of alumina nanoparticles to alter the properties of the polyamide layer formed during interfacial polymerization. The nanotemplated membranes have high resistance to organic and biological fouling, a property that is attributed to a change in the free energy of cohesion of the active layer. This simple membrane modification strategy, by impacting the intrinsic properties of the surface, can achieve long term fouling resistance and help mitigate the impacts of fouling in membrane-based desalination.

Nanoparticle-templated polyamide membranes for improved biofouling resistance

Naiara Mottim Justino[a,b], Denice Schulz Vicentini[a], Kiarash Ranjbari[b,c], Marion Bellier[b,c], Diego José Nogueira[a], William Gerson Matias[a], François Perreault[b,c]*

[a]Department of Sanitary and Environmental Engineering, Federal University of Santa Catarina, Florianópolis, SC, 88040-900 Brazil.

[b]School of Sustainable Engineering and the Built Environment, Arizona State University, Tempe, AZ, 85287-3005 United States

[c] Nanosystems Engineering Research Center for Nanotechnology-Enabled Water Treatment, Arizona State University, Tempe, Arizona, United States

Abstract

Applying an interlayer of nanomaterial to the support layer during interfacial polymerization results in a change in the polyamide (PA) properties that can be leveraged to improve the performance of desalination membranes. While studies have shown that permeability and selectivity can be increased using an interlayer of nanomaterials, the potential of using this approach to improve the PA properties relevant for fouling and biofouling is less understood. In this study, we investigated how using an interlayer of alumina nanoparticles (Al-NP) to template the interfacial polymerization process affects the fouling and biofouling propensity of thin film composite membranes. Performance was measured by static bacteria and protein deposition assays as well as dynamic reverse osmosis biofouling experiments. The low and medium Al-NP loadings were found to reduce bacteria and protein adhesion while, at a high Al-NP loading, both bacteria and protein adhesion increased. A similar trend was observed in dynamic fouling conditions, with the low and medium Al-NP loadings experiencing less flux decline and lower biofilm volume on the membrane compared to the control or high Al-NP membrane. The superior antifouling properties of these membranes were correlated with the change in the free energy of cohesion of the PA layer formed on the Al-NP interlayer. Our results demonstrate that using an interlayer of Al-NP can alter the PA surface chemistry in a way that reduces membrane fouling; however, there is a threshold loading of Al-NP beyond which fouling propensity increases due to the effect of Al-NP agglomeration on the PA morphology. These results provide useful insights into how NP can be added to the interlayer during interfacial polymerization to improve the performance of desalination membranes.

Keywords: Interlayer, alumina nanoparticles, antifouling, antimicrobial, surface free energy, reverse osmosis.

1. INTRODUCTION

The growing demand for freshwater by human activities, which include direct consumption, irrigation, and industrial uses, is putting an increasing pressure on conventional water sources [1]. As concerns arise over the sustainability of water supply, there is an accrued interest in producing clean water from alternative sources such as seawater, wastewater, or brackish water. These alternative sources are usually characterized by higher concentrations of salts and contaminants, which result in the need to use desalination processes in order to make these waters fit for use. Currently, the most widely used technology for desalination is reverse osmosis (RO) due to its high energy-efficiency and reliable performance compared to thermal methods [2]. Although RO currently dominates commercial desalination applications, it is still a costly process. The development of new membrane fabrication techniques that help mitigate the costs of RO operations can make desalination more accessible to a wider range of applications.

One of the main factors that contribute to the high operational cost of RO is membrane biofouling [3]. Biofouling consists in the adhesion and proliferation of microbes at the membrane surface, where they develop in an heterogeneous community enclosed in a matrix made of extracellular polymeric substances (EPS) [4]. Biofouling increases the pressure drop across the membrane module, resulting in the need to increase the applied pressure in order to maintain a constant permeate flux [5]. Biofouling also affects the permeate quality by the accumulation of ions at the membrane interface through cake-enhanced concentration polarization [6]. Beyond the

implications at the membrane stage, the operational aspects of biofouling control, such as feed pre-treatment, preventive overdosing of chemicals, and the down-time during cleaning all contribute to the high cost of RO [3,7]. Significant efforts have been made to improve the pretreatments [8], optimize the operational conditions [9], or modify the membrane surface properties [4] in order to reduce biofilm formation in RO systems.

Thin-film composite (TFC) polyamide (PA) membranes are the most widely used RO membranes [2,4]. PA TFC consists of a dense ultra-thin PA layer interfacially polymerized onto a porous support, usually polysulfone (PSU). Due to its high roughness, hydrophilicity, and abundance of carboxylic acid functional groups, the PA active layer is very prone to biofouling [10,11]. Reducing the initial interaction between bacteria and the PA surface is critical for biofouling control since microorganisms can multiply rapidly and secrete EPS after the initial adhesion, which makes the biofilm network difficult to remove [3]. Controlling bacterial adhesion is usually achieved by altering the surface characteristics that make a membrane susceptible to fouling: hydrophobicity, roughness, surface charge, surface free energy, and surface chemistry [4,12,13]. Surface modification methods are mostly based on the addition of hydrophilic materials on the PA layer [4,14] or on the addition of a coating of biocidal nanomaterials to the membrane [15].

The structure and chemistry of the support layer also play an important role on the interfacial polymerization (IP) process and thus on the characteristics of the resulting PA active layer [16]. The formation of PA by IP in a membrane support starts when aqueous diamine solution comes into contact with the support to allow diamine penetration. After removing the excess solution, the diamine-saturated support is immersed in an organic phase containing trimesoyl chloride (TMC). Since TMC is not soluble in water, diamine monomers diffuse to the water/organic interface and react with TMC to form the PA film [17]. In the conventional membrane

configuration, PA is formed over porous supports which confine the water/organic interface at the meniscus within the pores [18]. However, an interlayer material can also be used to manipulate the IP process and change the resulting properties of the active layer [18]. For example, a nanostructured interface can enable a more homogeneous distribution of the monomer solution across the interface and a more effective control of monomer release during IP [19,20].

Even though the role of the polymeric support surface in the formation of the PA layer has been established in earlier studies [21,22], the use of an interlayer medium to tailor the IP has only recently gained interest due to its promising results related to permeability and salt rejection [16]. Possible strategies to control the interfacial reaction include the use of carbon nanotubes [20,23,24], silver nanoparticles [25], and cellulose nanocrystals [26]. However, despite many studies reporting a change in surface properties known to be associated with biofouling propensity, such as hydrophilicity [23], morphology [19,20], and roughness [27], there is, to date, a lack of understanding on how the presence of an interlayer may affect biofilm formation on the resulting TFC membranes.

In this paper, we investigated the effects of an interlayer of alumina nanoparticles (Al-NP), added as a template to the IP process, on the fouling propensity of PA TFC membranes. The overarching objective was to understand how the addition of Al-NP in the interlayer influences the resulting PA properties and, consequently, membrane fouling. Using an *in situ* growth method to ensure a good dispersion of Al-NP on the support, three different concentrations of Al-NP were evaluated to determine the effect of Al-NP loading on the PA morphology, surface properties, and fouling propensity. Antifouling properties were measured by static bacteria and protein deposition assays as well as dynamic biofouling experiments in a bench-scale RO system. Our results demonstrate that Al-NP alter the IP process, which results in a change in the PA surface chemistry in a way that reduces membrane fouling without affecting the membrane performance. However,

there is a threshold loading of Al-NP beyond which the fouling propensity increases due to the effect of the high Al-NP density on the PA layer morphology. These results provide useful insights into how to use the NP in the interlayer of TFC membranes to improve the performance of RO desalination systems.

2. MATERIALS AND METHODS

2.1. Materials

Polysulfone beads (PSU, Mn 22,000), sodium borohydride, aluminum sulfate hydrate, and 1-methyl-2-pyrrolidinone (NMP) were obtained from Sigma-Aldrich (St. Louis, MO). The m-phenylenediamine (MPD) was obtained from Spectrum Chemical MFG Corporation (Gardena, CA). Isopar-G was obtained from Univar (Redmond, WA). Dopamine hydrochloride (DPA) was obtained from Alfa Aesar (Ward Hill, MA). Fluorescein isothiocyanate labelled bovine serum albumin (FITC-BSA) was obtained from Thermo Fisher Scientific. Live/Dead™ BacLight™ Bacterial Viability kit was obtained from Invitrogen (Eugene, OR). Phosphate buffered saline tablets was obtained by Fisher Bioreagents™ Fairlawn, NJ. Isopropyl alcohol was obtained from Macron (Radnor, PA). Agar and Luria-Bertani Broth (LB) were obtained from VWR (Solon, OH). Tris(hydroxymethyl) aminomethane (Tris) was obtained from Acros (NJ). 1,3,5-Benzenetricarbonyl trichloride (TMC) was obtained from Tokio Chemical Industry (Portland, OR).

2.2. Membrane preparation

2.2.1. Polysulfone support

Asymmetric PSU membranes were prepared by phase inversion via immersion precipitation. PSU pellets were dissolved in NMP (16.3% w/w) at 50 °C by constant stirring for 3 days, and kept still for 1 h of degassing. The resulting solution was spread on a glass plate using a casting knife to obtain a thickness of 110 μm. Before the plate immersion in a non-solvent coagulation bath (DI water), the coated film was allowed to evaporate in ambient air (~23 °C) for 30 s. After polymer precipitation in DI water, the membrane was put into 50% ethanol/DI water for 30 min to ensure complete solvent removal. Membranes were stored in 1% sodium bisulfite/DI water solution at 4 °C DI water at least 24 h prior to use.

2.2.2. Polydopamine coating

PSU support surface was coated with polydopamine to enhance interfacial interactions between the alumina nanoparticles (Al-NP) and the polymer matrix [28]. Dopamine solution was prepared by dissolving dopamine hydrochloride in Tris-HCl buffer solution (15 mM, pH 8.6) at a concentration of 0.5 g/L. Samples of PSU membranes (14 × 10 cm) were placed on a glass plate and fixed onto the frames to ensure the reactant solution only made contact with the top surface. The dopamine solution was self-polymerized on the membrane surface for 1 h at room temperature. After PDA coating, the resulting PSU-PDA membranes were washed with DI water several times and kept in DI water at 4 °C.

2.2.3. *In situ* formation of Al-NP

Al-NP were formed *in situ* using aluminum sulfate ($Al_2(SO_4)_3$) as a salt precursor and sodium borohydride ($NaBH_4$) as the reducing agent. With the PSU-PDA membranes fixed in the frame (see Section 2.2.2.), 30 mL of $Al_2(SO_4)_3$ solution (6.25, 12.5 or 24 mM of Al^{+3}) reacted with the PSU-PDA layer for 3 min. Then, 30 mL of $NaBH_4$ solution (18.75, 37.5 or 72 mM) was added

into the $Al_2(SO_4)_3$ solution and allowed to react for 7 min. After the formation and deposition of Al-NPs on the membrane surface, the solution was removed and the prepared *in situ* Al-NP modified membrane was rinsed thoroughly with DI water, then stored in DI water.

2.2.4. Preparation of polyamide selective layer

The PA active layer was formed on control (PSU-PDA) and Al-NP incorporated membranes via IP. First, a 2% wt MPD aqueous solution was poured onto the membrane surface for 1 min before draining it off. The excess MPD was removed with air knife. Immediately, the MPD-soaked membrane substrate was immersed into a 0.15% w/v TMC/Isopar-G solution for 30 s. During this step, the MPD in the membrane diffused out of the membrane and cross-linked with TMC at the water/solvent interface to form the PA active layer on the membrane. The membrane was rinsed with Isopar-G to remove unreacted monomers. To complete the polymerization process, membranes were cured at 50 °C for 10 min. After PA crosslink, all membranes were washed thoroughly with DI water and kept in DI water at 4 °C. The control membrane without Al-NPs was referred as MC and Al/PA membranes with low (6.25 mM), medium (12.5 mM) and high (24 mM) Al^{+3} concentrations used to form the Al-NP intermediate layer were referred as ML, MM and MH, respectively. Final membrane thickness, measured by Optical Coherence Tomography (OCT, GANYMEDE II, Thorlabs) was 118 ± 14 μm did not different significantly between membranes.

2.3. Membranes and NP-Al NP characterizations

Formation of Al-NPs on the PDA layer and morphology of the membrane surface were characterized by field emission scanning electron microscopy (FESEM) (JEOL, JSM-6701F) at an acceleration voltage of 15 kV. Membrane cross-sections were obtained by an argon ion beam

cross-section polisher (JEOL, SM-09010). To avoid charging under the argon or electron beams used during polishing and FESEM analysis, respectively, all samples were coated with a gold layer using a high vacuum sputter-coater (LEICA, EM SCD 500). Al-NP size and distribution were determined using ImageJ and Statistica® software, respectively. Energy-dispersive X-ray (EDX) analyses were conducted to detect aluminum in the membranes.

Surface roughness of membranes was measured via AFM (Multimode 8, Bruker). Image analysis was done using the Nanoscope Analysis version 1.9 software. X-ray photoelectron spectroscopy (XPS) was done on a VG 220i-XL (Thermo Fisher Scientific Ltd. Hampton, NH) equipped with a monochromated Al K-alpha X-ray source. The data was analyzed using the CasaXPS software (version 2.3.18). The density of carboxyl groups on the membrane surface was quantified by the silver ion binding method as described by Chen et al. [29]. The binding procedures are fully detailed in the Supplementary Information (SI) S1. Silver concentrations were determined by inductively coupled plasma mass spectrometry (ICP-MS). Since it is assumed that each eluted silver ion corresponds to one ionized carboxyl group, the ionized carboxyl group per membrane surface area [R-COO$^-$] can be converted using Equation 1.

$$[\mathrm{R - COO -}] = \frac{M_{Ag} V_{el} N_A}{A} \quad (1)$$

where M_{Ag} is the silver concentration converted to molar concentration, V_{el} is the elution volume, N_A is Avogadro's number, and A is the membrane's surface area (coupon single-sided area).

Hydrophobicity/hydrophilicity of membrane surfaces were measured by water contact angle (WCA) and surface free energy of cohesion (ΔG_{sw}) using sessile drop contact angles (CA). CA were taken by using an Attension Theta (BiolinScientifin, Gothenburg, Sweden) and a 1001 TPLT Hamilton syringe (Reno, NV). Six different membrane spots were measured. For each

measurement, ~200 data points were recorded over 10s and these values were averaged into a final mean. Nanopure water was used for WCA, while apolar diiodomethane, polar nanopure water, and ethylene glycol standard liquids were used to determine surface tension parameters (γ^{LW}, γ^{+}, γ^{-} and γ^{AB}) using Young–Dupré equation with roughness correction factor (Cassie–Baxter equation) (Equation S1). The surface tension parameters calculations are presented in detail in Supplementary Information (S2). The determination of interaction energies between membranes and foulants was based on XDLVO theory in terms of ΔG_{sw} (Equation 2), which provides quantitative insight into the stability of a solid (membrane and foulants molecules) in water [30], and by interfacial free energy of adhesion (ΔG_{ad}^{tot}) (Equation 3) between membrane surface and foulant in water. ΔG_{ad} is divided into three components: Lifshitz-van der Waals interaction energy (ΔG^{LW}) (Equation 4), Lewis acid-base interaction energy (ΔG^{AB}) (Equation 5), and electrostatic force (ΔG^{EL}) energy (Equation 6)[31].

$$\Delta G_{sw}^{tot} = \Delta G_{sw}^{LW} + \Delta G_{sw}^{AB} + \Delta G_{sw}^{EL} \quad (2)$$

$$\Delta G_{sw}^{LW} = -2\left(\sqrt{\gamma_s^{LW}} - \sqrt{\gamma_l^{LW}}\right)^2 \quad (3)$$

$$\Delta G_{sw}^{AB} = -4\left(\sqrt{\gamma_s^{+}} - \sqrt{\gamma_l^{+}}\right)\left(\sqrt{\gamma_s^{-}} - \sqrt{\gamma_l^{-}}\right) \quad (4)$$

$$\Delta G_{sw}^{EL} = \frac{\varepsilon_0 \varepsilon_r \kappa}{2}(\xi_s^2 + \xi_l^2)\left[1 - \coth(\kappa h_0) + \frac{2\xi_s \xi_l}{\xi_s^2 + \xi_l^2}\operatorname{csch}(\kappa h_0)\right] \quad (5)$$

$$\Delta G_{ad}^{tot} = \Delta G_{ad}^{LW} + \Delta G_{ad}^{AB} + \Delta G_{ad}^{EL} \quad (6)$$

$$\Delta G_{ad}^{LW} = 2\left(\sqrt{\gamma_l^{LW}} - \sqrt{\gamma_m^{LW}}\right)\left(\sqrt{\gamma_f^{LW}} - \sqrt{\gamma_l^{LW}}\right) \quad (7)$$

$$\Delta G_{ad}^{AB} = 2\sqrt{\gamma_l^+}\left(\sqrt{\gamma_m^-}+\sqrt{\gamma_f^-}-\sqrt{\gamma_l^-}\right)+2\sqrt{\gamma_l^-}\left(\sqrt{\gamma_m^+}+\sqrt{\gamma_f^+}-\sqrt{\gamma_l^+}\right)-2\left(\sqrt{\gamma_m^+\gamma_f^-}-\sqrt{\gamma_m^-\gamma_f^+}\right) \quad (8)$$

$$\Delta G_{ad}^{EL} = \frac{\varepsilon_0\varepsilon_r\kappa}{2}(\xi_m^2+\xi_f^2)\left[1-\coth(\kappa h_0)+\frac{2\xi_m\xi_f}{\xi_m^2+\xi_f^2}\mathrm{csch}(\kappa h_0)\right] \quad (9)$$

The subscripts s, l, m, and f represent the solid (membrane or foulant), liquid, membrane surface, and foulant, respectively. The ε0 is vacuum permittivity, εr represents the dielectric permittivity of spending fluid, κ is the inverse Debye length, ξ is the zeta potential, and h_0 is the is the minimum separation distance. Zeta potential measurements were taken using a ZetaCAD® analyzer (CAD Instruments, Les Essarts-le-Roi, France). The streaming potential determination was carried out with a solution containing 5 mM KCl and 0.1 mM $KHCO_3$ at pH 6.5, the same pH as used during bacteria deposition assays (see section 2.6).

2.4. Membrane transport properties

Membrane permeability and selectivity were evaluated using a bench-scale cross-flow filtration system at constant room temperature (25 °C). The effective area of the membrane was 34 cm^2. Pre-wetted membranes were compacted in deionized water at 15.5 bar until the permeate flux reached a stable value (~3h). The cross-flow velocity was kept constant at 37.8 cm/s. After stabilization, NaCl was added from a 5M stock solution to reach a final value of 2,000 ppm in the feed reservoir. Permeate flux was recorded every 60 s using a liquid flow meter (Sensirion SLI-2000, CMOSens®). Pure water flux J ($L/(m^2\ h)$) was calculated as J = V/(t A), where V is the volume of permeate (L) collected over a period of time t (h), and A is the effective area of the membrane (m^2). Subsequently, the salt rejection (R) was determined as R = 1 – Cp/Cf, where Cp

and Cf are the conductivity of the permeate and feed waters, respectively, measured with a Orian Versa Star (Thermo Fisher Scientific, Waltham, MA) conductivity probe.

2.5. Antimicrobial surface properties

Bacterial deposition on membrane surfaces was evaluated by counting live and dead *Pseudomonas aeruginosa* (*P. aeruginosa*, ATCC 15692) cells, a model bacterium for biofilm formation. An overnight culture of bacteria grown in LB was diluted in fresh LB (1:25) and grown in an incubator at 37ºC and 100 rpm constant agitation until it reached an optical density (OD600nm) of 1.0 (~2 h) , indicating late exponential phase (10^9 cells/mL). Bacteria were washed from LB 3 times with a 0.9% NaCl in nanopure water. Membrane samples were cut in 2 cm diameter coupons and placed in plastic holders in a way that only allowed contact of the solution with the surface. A 3 mL volume of bacteria/0.9% NaCl nanopure water solution (~10^7 cells/mL) was placed in contact with the membrane surface for 3 h. Samples were then removed, gently washed with 1 mL NaCl solution. The cells attached were dyed using Live/Dead™ BacLight™ Bacterial Viability kit from Invitrogen, according to the manufacturer's specification. Live (green) and dead (red) bacteria cells were imaged in Leica DM6 epifluorescence microscope (Leica Microsystems Inc. Buffalo Grove, IL) and counted using ImageJ software.

2.6. BSA adhesion

The antifouling property of membranes was evaluated using FITC-BSA, a model bovine serum albumin (BSA) protein conjugated with Fluorescein isothiocyanate (FITC) under static adsorption conditions [14]. Samples were placed in plastic holders as described in Section 2.5. An aqueous solution of 0.05 mg/mL FITC-BSA (2 mL) in phosphate buffer solution (PBS, pH 7.4) was placed in contact with the membranes' surface for 3 h in a dark environment. The FITC-BSA

was removed and the surface was gently washed with fresh PBS solution. The membrane sample was then placed on a glass slide for epifluorescence microscopy analysis. The intensity of green fluorescence of microscopy images was measured using ImageJ software. A membrane not exposed to FITC-BSA was used as a control to assess the background green fluorescence of the membrane. All epifluorescence measurements were made under the same acquisition conditions to be able to compare the fluorescence intensities between samples.

2.7. Dynamic biofouling

The biofilm formation on the membranes under dynamic RO conditions was evaluated by filtration in a bench-scale cross-flow unit. Pre-wetted membranes (20% isopropyl, 20 min) with 34 cm^2 effective area were loaded in the membrane cell and compacted until the flux reached stable values (~7 h). The system was operated at constant pressure (27.6 bar), temperature (20 °C) and cross-flow (1 cm/s). Permeate flux was recorded every 60 s using a liquid flow meter (Sensirion SLI-2000, CMOSens®). Biofouling was investigated using synthetic secondary wastewater mixed with *P. aeruginosa* at 2.5 x 10^8 cells/L concentration in a 20 L tank (see Table S3 for details). Permeate water was returned to the reservoir to maintain a constant salt concentration. The solution was circulated for 45 h at room temperature and biofouling was evaluated by change in flux over time. After 45 h, membranes were collected and biofilms were imaged using OCT imaging (GANYMEDE II, Thorlabs) at four different regions. The biofilm cross-section area was quantified by ImageJ.

2.8. Data analysis and statistics

The data shown represents the means of three independent samples. Significant differences between them were determined by ANOVA, followed by a Tukey post-hoc test with $\alpha < 0.05$ using OriginPro 2018 software. Statistically significant different samples were indicated using different letters in the figures. Linear regression analyses between the surface properties of the different membranes and deposition of *P. aeruginosa* cells or BSA proteins were done using the "stats" package of the R statistical software (v. 4.0.2). A forward selection approach was used, with predictors being added one at a time to identify the parameters to be included in a multiple regression model. Independent variables that are intrinsically correlated with each other (i.e. Rq and Rmax, ΔG_{sw} and WCA) were not used when developing a multiple regression model.

3. RESULTS AND DISCUSSION

3.1. Characterization of membrane and Al-NP

The FESEM micrographs of the PSU cross-section show the formation of a substrate with an overall thickness of 109 ± 0.18 μm and a typical asymmetric porous structure composed of a thin dense layer on the top and a finger-like porous sublayer extending from the top to the bottom, forming macrovoids in the support (Figure 1A). PSU surface showed micropores of 0.49 ± 0.13 μm average (Figure 1B), but the dense top layer facilitated the formation of a continuous PDA coating at membrane surface, as illustrated in Figure 1C. Some PDA nanoaggregates (~50 nm) are observed distributed on the PDA coating, which are strongly bound to the PDA layer by catechol groups [32].

The PDA coating was used to anchor the Al-NPs on the support before IP. Membranes modified by *in situ* formation of Al-NP at low, medium and high concentrations of $Al_2(SO_4)_3$ are

shown in Figure 1D. The formation of Al-NPs can be observed by the presence of sphere-like structures on the PDA layer, which increase in numbers as the $Al_2(SO_4)_3$ concentration increases. Additionally, EDX analyses show that the atom % of Al increases significantly ($p<0.05$) as the concentration of precursor increases from the ML to the MH conditions (Figure 1E). Differences are also observed in the size and dispersion of Al-NPs formed on the PDA coating at different Al-NP loading, with average particle diameters of 67.2 ± 29.5, 55.0 ± 21.5, and 121.5 ± 101.2 nm for the ML, MM, and MH conditions, respectively (Figure 1F). The medium concentration formed the most homogeneously sized and well-distributed Al-NPs on the PDA layer. The similarity between the distribution of PDA nanoaggregates and Al-NPs at the medium concentration (Figure 1C and 1D) suggests that PDA nanoaggregates play a role in Al-NP formation. Several studies identified PDA nanoaggregates as anchor sites for the growth of NPs [33,34]. PDA facilitates the formation of Al-NPs by spontaneous interactions between Al^{3+}, which are in the solution phase at pH 3.5, with the negatively charged catechol groups that are in high density in PDA nanoaggregates [35]. They form strong coordination bonds but in a slow reaction that requires a long contact time [32]. In this work, Al-NP formation was based on a two-step process that involved adsorption and *in situ* reduction of the precursor to Al-NP. First, the $Al_2(SO_4)_3$ solution was put in contact with the PDA surface to induce the adsorption of Al^{+3}. Then, a reducing agent ($NaBH_4$) was added to accelerate the Al-NP formation *in situ* [36]. At higher Al^{+3} concentration in the solution, there are more chances to attach to the catechol groups, which result in more Al-NPs formed on the PDA surface. However, at the highest $Al_2(SO_4)_3$ concentration, the membrane showed Al-NP aggregates with a wide range of sizes (Figure 1F). By controlling the Al-NP precursors' concentrations to the low and medium values used in this work, it was possible to limit Al-NP agglomeration on the PDA layer.

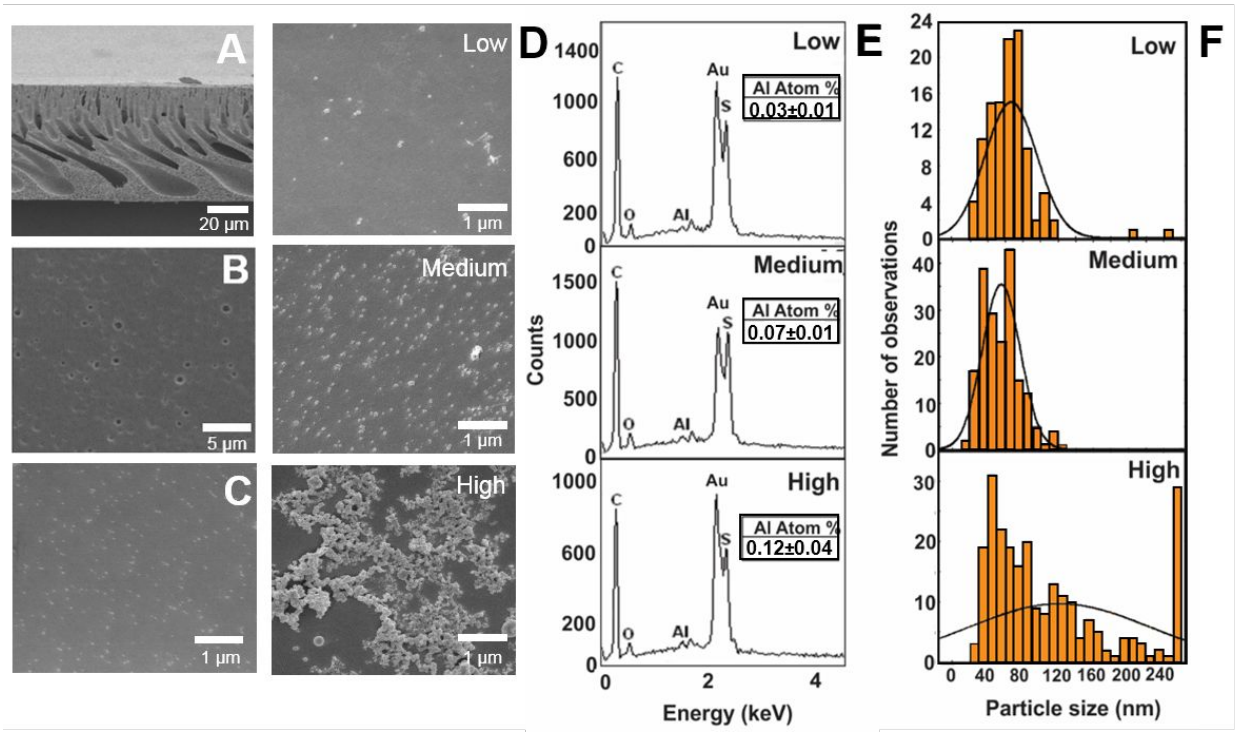

Figure 1. Characterization of membrane support, TFC membrane and Al-NP formed over PDA-PSU. (A-F) FESEM micrographs of (A) PSU support cross-section, top view of (B) PSU surface, (C) PDA coated PSU surface, (D) Al-NP on PDA-PSU at low, medium, and high concentration. (E) Gaussian curve showing size distribution of NP-Al of D images and (F) the corresponding EDX spectra confirming the formation of Al-NP.

The PDA-coated PSU support, with or without Al-NP, were used for IP of the PA layer to form TFC membranes. Figure 2A depicts the surface morphology of PA control membrane formed by IP, showing small discrete nodules and large "belt-like" structures formed by the overlap and fusion of PA leaves [37]. The morphology of the PA layer formed on the Al-NP coated PDA-PSU reveals differences in the width and length of PA protuberances. ML shows more nodules and less belt structures (Figure 2B). On the other hand, at the higher concentration of loaded Al-NP, the belt-like features became larger and more interconnected (Figure 2D). It is important to note the absence of belt structures in MM (Figure 2C), where the PA layer only shows extended leaves and

nodules. The reduction of belt-like structures in ML and MM can be attributed to the homogeneous distribution of hydrophilic Al-NPs on the support, which retains MPD molecules and slows down MPD diffusion to react to TMC during IP [22]. Further analysis using AFM imaging revealed that, as the Al-NP loading on the support increased, the roughness of the PA surface increased. This can be explained by the different surface morphologies formed due to the added roughness of the Al-NP layer on the support, especially for the MH condition where high Al-NP aggregation occurred. Different from the findings of Ma et al. [37], here, the flat feature of the belt structures did not result in a decrease in surface roughness. This discrepancy is most likely due to the lower interconnection between the belt structures, which were not enough to cover the surface and resulted in PA peaks formed by isolated belts that increased the roughness. Top surface AFM profiles (Figure 2E) give an idea on how surface structures are vertically present. Higher peaks are observed in MM and MH, which are related to the extended leaves and belts, respectively, as a consequence of the Al-NP interlayer. Representative 3-dimensional AFM images of the different membrane surfaces are shown in Figure S1. The presence of PA peaks at higher Al-NP loading resulted in higher values of the Rq, Ra, and Rmax roughness parameters as the Al-NP loading increased (Figure 2F). The increase in roughness was statistically different from the control (MC) only for the highest Al-NP loading (MH); however, a trend can be observed between the Al-NP loading and the surface roughness of the PA formed on the support.

.

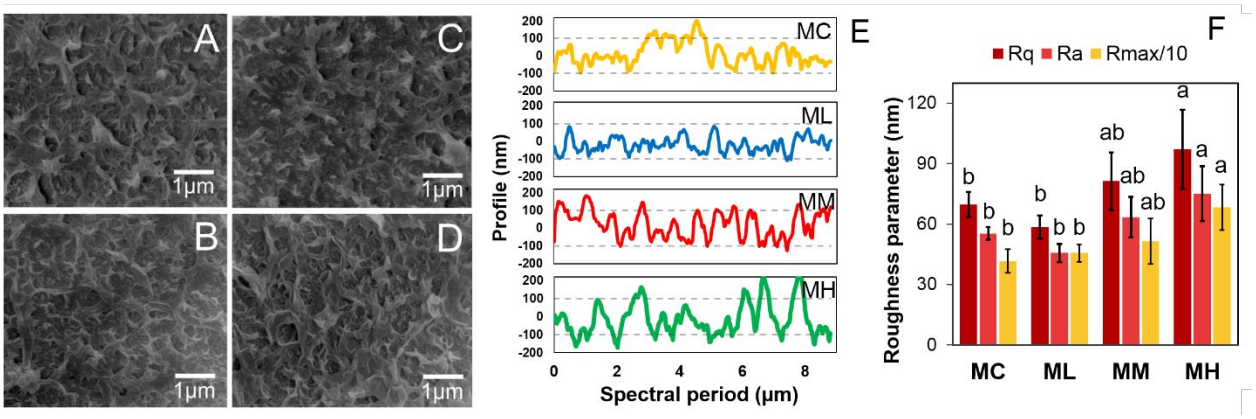

Figure 2. Surface morphology and roughness of the control and modified membranes. (A-D) Top surface FESEM micrographs of (A) MC, (B) ML, (C) MM and (D) MH. (E) Top surface AFM profiles and (F) rough mean square (Rq), average roughness (Ra) and maximum roughness divided by 10 (Rmax/10) surface roughness parameters. Lower case letters indicate statistical significance (different letters representing statistical difference) (p-value <0.05), determined by One-way ANOVA (post hoc Tukey).

3.2. Physicochemical changes in membrane surface

The change in the PA morphology may indicate a change in the physicochemical properties of the active layer. Therefore, the membranes were further characterized to understand how the addition of the Al-NP changed the surface properties of the membrane. FTIR spectroscopy was used to characterize the structure of each layer of the produced membranes and XPS was conducted to determine the chemical surface structure of the control PA and PA formed over the Al-NP interlayer. Because of the depth of penetration of FTIR (1-3 μm) and the thickness of the PSU support compared to the other layers of the PA TFC membrane, the FTIR spectra show dominant peaks associated primarily with the PSU support such as the 1150 cm^{-1} (symmetric O=S=O stretching), 1250 cm^{-1} (asymmetric C-O-C stretching), 1290 cm^{-1} (S=O stretching), 1325 cm^{-1}

(asymmetric O=S=O stretching), 1488 cm^{-1} (CH_3-C-CH_3 stretching), 1405 cm^{-1} (C=C aromatic ring stretching), and 1600 cm^{-1} (C=C symetric and asymmetric stretch) peaks (Figure 3A) [38]. The characteristic absorption bands corresponding to PDA would found at 1610 cm^{-1}, for aromatic rings stretching vibrations and N–H bending vibrations, and 3400 cm^{-1} for the catechol –OH and N–H groups [39]. For Al-NP, typical FTIR absorption bands include the 1600 cm^{-1} (Al-O) and 3400 cm^{-1} (O-H stretching) peaks [40]. However, in both PDA and Al-NP functionalized support and TFC membranes' spectra, the peaks associated with PDA and Al-NPs are not observed. These results are similar to previous studies done on TFC composite membranes[39,41] and is attributed to the low amount of Al-NP and the very thin PDA layer added to the membranes compared to the thick PSU support as well as the overlap the PDA and Al-NPs peaks with the strong C=C band of PSU at ~1600 cm^{-1}. It should be noted that successful PDA functionalization was observable to the eye by a darker coloration of the PDA-coated PSF while the presence of Al-NPs was confirmed by SEM, as shows above (Figure 1).

After IP, the addition of the PA resulted in the apparition of the characteristic amide band peaks of 1546 cm^{-1} (amide II stretching), 1610 cm^{-1} (aromatic ring breathing), and 1660 cm^{-1} (C=O stretching), as well as a peak at 1710 cm^{-1} related to C=O stretching peak of carboxylic acid (Figure 3A), confirming the successful formation of PA thin film. In addition, the presence of a broad band around 3400 cm^{-1} is related to the overlapping bands of O-H stretching of carboxylic groups and N–H vibration associate to amide II of polyamide layer [42]. The spectra of MC, ML, MM and MH (Figure 3B) is showing that the C=O stretching peak of carboxylic acid (1710 cm^{-1}) and the broad band around 3400 cm^{-1} both diminish in Al-NP loaded membranes compared to MC as Al-NP loading increases. This reduction of carboxylic functional groups is an indicative of increased

cross-linking in the PA layer. Furthermore, the overall reduction in PA peak intensity for the PA layer formed over the Al-NP interlayer suggests the formation of a thinner and denser PA layer.

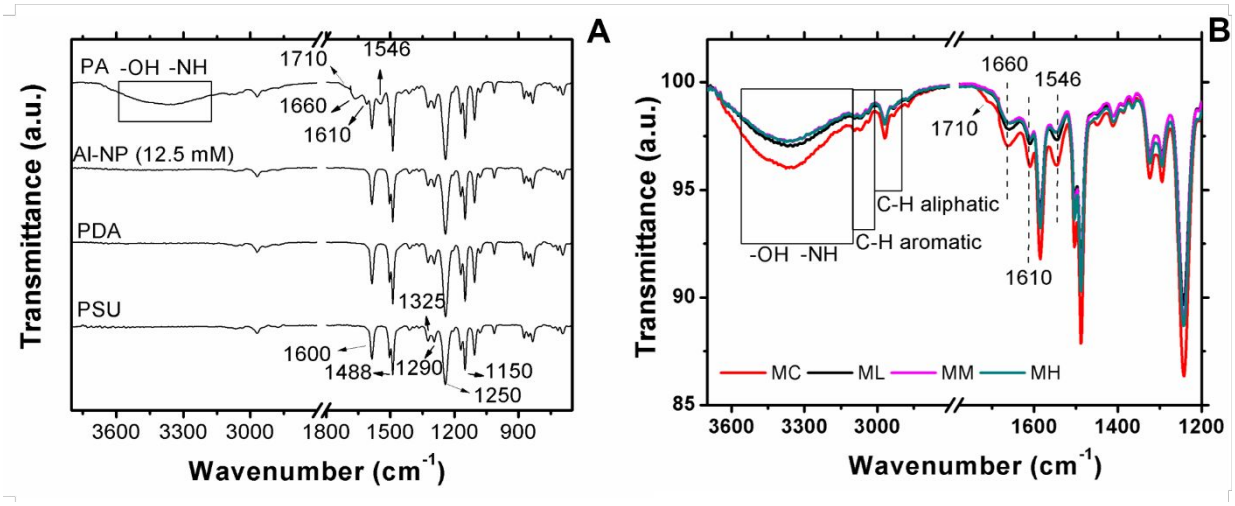

Figure 3. FTIR spectrum identifying the different functional groups of (A) each layer of the prepared membranes and (B) comparing the membrane with (ML, MM and MH) and without (MC) the Al-NP interlayer.

Change in the chemical structure of the PA induced by the addition of the Al-NP layer was also determined by deconvoluting the C1s peak of the XPS spectrum (Figure 4B-E). Detail information on atomic composition and chemical states is present in Table S4. The C1s analyses show a decrease in the relative contribution of the 288.9 eV peak, associated with amide and carboxyl groups in Al-NP loaded membranes. The O1s peak deconvolution of XPS analysis presented the N-C=O from the IP reaction of the acyl chloride groups of TMC with MPD, and the O–C=O bond, from the carboxyl groups originating from the hydrolysis of the unreacted acyl chloride groups of TMC molecule, characteristics of PA structure (Figure S2). Therefore, higher N-C=O over O-C=O ratio stands for a higher cross-linking degree of PA layer. The increase in Al-NP loaded result in the decrease in carboxylic acid peak contribution (533.1 eV) from 38.8% in MC to 33.8%, 28.8%, and 7.50% in ML, MM, and MH, respectively, confirming the reduction of

carboxylic acid showed in FTIR analysis and the increase of cross-linking degree. This result suggest that the presence of the Al-NP influenced the PA formation. The higher cross-linking degree of Al-NP loaded membranes can be explained by the high hydrophilicity of the Al-NP interlayer, which retains more MPD molecules and slows down the amide monomer diffusion into the organic phase during IP. The increase in amide monomers creates a MPD-rich and TMC-lean environment in the interface and makes MPD more available to cross-link with TMC to form denser, thinner, and more cross-linked structures [43–45]. Moreover, the O–H groups of NP-Al can react with the acyl chloride groups of the TMC, reducing the carboxyl group density and decreasing the thickness of the PA layer [46]. Dai et al., in their review of interlayer-tailored PA membranes, reported that due to the MPD retention/diffusion capability of interlayers, the PA thickness of interlayer-based TFC membranes is typically >60% thinner than membranes prepared by conventional IP [45]. Lower PA thickness can lead to an increase in water permeability. The membrane permeability measurements, done in a cross-flow filtration apparatus, showed an increase in flux for the Al/PA membranes compared to the control, with significantly higher flux at the MH condition compared to MC. This increased in flux did not compromise the salt rejection, which remained between ~90-92.5% for the different membranes with no significant differences between membranes (Figure S3). The higher flux can be attributed to (i) the direct role of the Al-NP interlayer in creating water transport pathway and (ii) its indirect effect through its influence on the PA formation (i.e., decrease in PA thickness and increase of membrane surface roughness) [25,43]. It should be emphasized that although the performance of these hand-cast Al/NPs membranes is comparable to other handcast composite membranes tested under comparable conditions of pressure and salinity,[47–50] the overall performance of the Al/PA membranes remain low compared to the state-of-the-art commercially available membranes, which typically features >95-99% salt

rejection. Therefore, further optimization of the interlayer-templated IP will be needed in future work for them to compete with commercially-made TFC membranes.

The reduction of O-C=O by the addition of Al-NP to the support during IP can have important implications for the fouling propensity of the PA surface, since the density of carboxyl groups on the surface, which is a result of the hydrolysis of unreacted acyl chloride groups during IP, has been shown to influence the fouling propensity of TFC membranes [51]. In the presence of calcium ions, which are common in secondary effluents, carboxyl groups of membrane surface can form calcium bridges with organic foulants, bacteria, and EPS, strengthening their binding to the membrane surface [11,52]. Given the importance of carboxyl group density on the fouling behavior of PA TFC membrane, we provided additional confirmation of the reduction in carboxyl group by a complementary quantitative assay based on the affinity of silver to carboxyl group and their quantification by ICP-MS after elution [29]. The silver binding assay confirmed the decreasing trend in carboxyl density from 2.54 carboxyl sites/nm^2 in MC to 1.4 sites/nm^2 in MH, at the highest Al-NP loading (Figure S4).

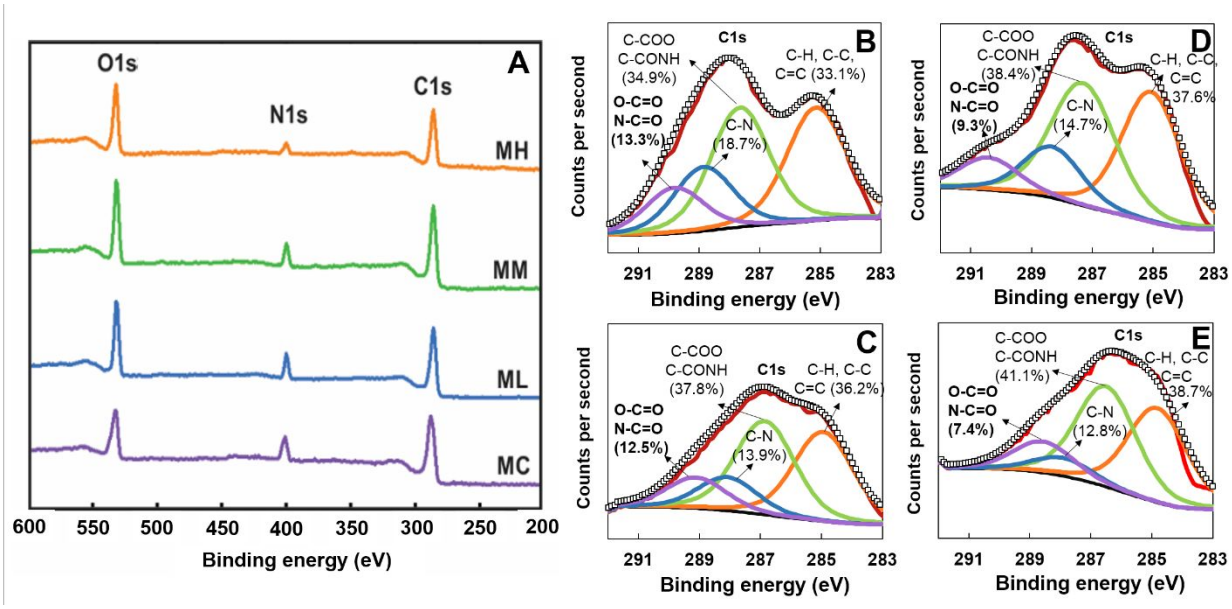

Figure 4. Surface changes in membranes. (A) XPS survey scan, (B-E) C1s XPS spectrums of

(B) MC, (C) ML, (D) MM, and (E) MH, identifying the relative reduction of carboxylic acid groups.

The change in surface chemistry induced by the Al-NPs will affect the membrane surface properties associated with hydrophilicity and surface free energy. These properties are well-known characteristics associated with the propensity of foulants such as proteins and bacteria to adhere to the surface [12,31]. The WCA of MC surface was 73.0° ±3.5 (Table S1), which is relatively hydrophobic. Only at high concentration (MH), the Al/PA membranes presented variation on WCA, turning more hydrophobic (89.9° ±5.7). Since WCA is influenced by the surface roughness, which was shown to change with the different Al-NP loading (Figure 2F), the hydrophilicity/hydrophobicity of the different membranes was confirmed by determining the free energy of cohesion (ΔG_{sw}), which uses surface tension parameters corrected by a surface roughness correction factor (r) in the ΔG_{sw} calculation (Equation S1 and Table S2). The sign and magnitude of ΔG_{sw} is a quantitative measure of stability of foulant molecules in water [53]. When the ΔG_{sw} is positive, the surface is considered hydrophilic while negative ΔG_{sw} values is equivalent to a hydrophobic surface [30,53]. The ΔG_{sw} results show that all membranes possess a hydrophobic surface. However, there was a slight decrease in hydrophobicity for the ML and MM membranes with ΔG_{sw} values of -40.4 and -41.3 mJ/m^2, respectively, while the MC membrane had a ΔG_{sw} value of -49.4 mJ/m^2. Similar to WCA results, high Al-NP loading in the interlayer resulted in an increase in hydrophobicity, with the MH membrane having a ΔG_{sw} of -71 mJ/m^2. Meanwhile, the foulants *P. aeruginosa* and BSA are considered hydrophilic based on their positive values of ΔG_{sw}, 21.6 and 24.5 mJ/m^2, respectively. Incorporating an hydrophilic interlayer is a common strategy to improve the hydrophilicity of PA surface although the mechanisms are still poorly understood [25,54]. The increase of hydrophilicity on ML and MM could be attribute to the hydrophilic nature of

Al-NP [55,56]. On the other hand, when Al-NP concentrations increase and agglomerates are formed on the support, the PA surface becomes rougher with belt-like structures that can trap air pockets in the structure and reduce the wettability of the surface[12]. Therefore, for optimal surface wettability, Al-NP loading needs to be controlled to avoid agglomeration.

The interaction force between the membrane surface and the foulants in water was determined based on the extended DLVO theory of surface free energy of adhesion (ΔG_{ad}), which considers the Liftshitz-van der Waals (LW), Lewis acid-base (AB) and electrical double layer (EL) surface energies. Two different types of foulants were considered to evaluate the fouling propensity of the different membranes: the biofilm-forming model bacterium *P. aeruginosa* and the model protein foulant BSA. Figure 5 shows the total of the surface free energy of adhesion (ΔG_{ad}^{tot}) and the contribution of the adhesion components LW (ΔG_{ad}^{LW}) and AB (ΔG_{ad}^{AB}). The EL component (ΔG_{ad}^{EL}) was not found to account for the total ΔG_{ad} because it showed insignificant contribution compared to LW and AB energies. Also, the zeta potential values of membranes were very similar (~-10 mV at pH 6.5), suggesting no influence of the Al-NP loading on membrane surface charge. The ΔG_{ad}^{EL} and zeta potential values are shown in Table S5. When Al-NPs are added to the interlayer, the increase in ΔG_{ad}^{tot} towards less negative values in ML and MM compared to the control indicates a decrease in attraction between the membrane surface and both bacteria and protein. On the other hand, the remarkably negative ΔG_{ad}^{tot} of the MH membrane suggests a surface more prone to fouling by proteins or bacteria.

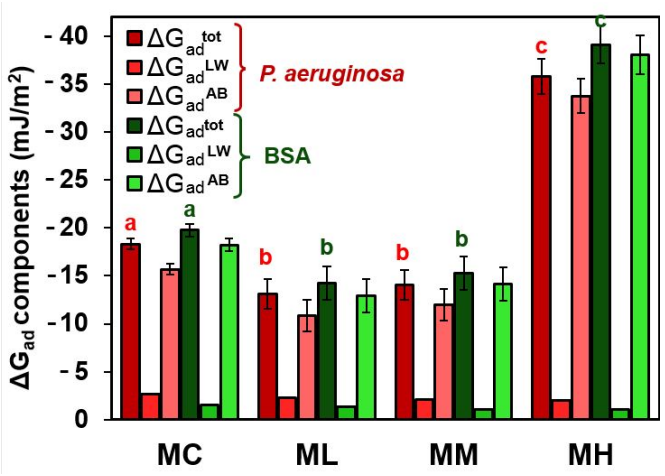

Figure 5. Surface free energy of adhesion (ΔG_{ad}) between membrane surface and the foulants *P. aeruginosa* and BSA (more negative ΔG_{ad} values indicates more attraction). Lower case letters indicate statistical significance (different letters representing statistical difference) (*p*-value <0.05), determined by One-way ANOVA (post hoc Tukey).

The changes in adhesion forces by the addition of the Al-NP interlayer mainly correlates with the acid–base interactions (ΔG_{ad}^{AB}). The negative values of ΔG_{ad}^{tot} and ΔG_{ad}^{AB}, and the relative low polarity of membrane and foulants compared to the strong polar (AB) energy of cohesion between water molecules, indicate that the major adhesion force between membrane and foulant is due to "hydrophobic interaction" [57]. This interaction is governed by the AB component of the energy of cohesion of water, which is composed of electron-donor (-) and electron-acceptor (+) functionalities. The presence of more electron-donor functional groups, represented by the surface tension (γ^-) in ML and MM (7.7-7.1 mN/m) compared to MC (5.1 mN/m), increased the interaction with γ^+ of water (25.5 mN/m) (Table 1). The increase of electron-donor functionality of ML and MM may be related to the interfacial hydroxyl groups present on the Al-NP [46,56]. The higher interaction with water reduces the hydrophobic interaction and forms an energetic barrier that prevents the adhesion of *P. aeruginosa* and BSA. MH, in the other hand, presents almost no electron-donor groups, which reduces the interaction with water and favors the interaction between

its electron-acceptor functional groups (1.7 mN/m) and electron-donor groups of *P. aeruginosa* and BSA (39.5 mN/m). This results in a substantially higher ΔG_{ad} in MH compared to the other membranes. In addition, *P. aeruginosa* and BSA have similar monopolar electron-donor functionalities ($\gamma^+ \approx 0$; $\gamma^- = 39.5$ mN/m) that could result in similar values of ΔG_{ad}, but the adhesion is slightly more pronounced for BSA. This is probably because BSA has sites with easy mobility and strong electron donor carbonyl groups that interact with discrete electron-acceptor on the membranes [57]. These results highlight the important role of membrane hydrophilicity, represented by γ^-, in membrane/water/foulant interactions.

Table 1. Thermodynamic characteristics of the membrane surfaces, foulants and water. Lifshitz-van der Waals surface tension (mN/m) (γ_s^{LW}), Lewis acid-base surface tension (γ_s^{AB}), electron-acceptor surface tension component (γ_s^+) and electron-donor surface tension component (γ_s^-), total surface tension (γ_s^{tot}) and surface free energy of cohesion ΔG_{sw}.

	γ^{LW} (mN/m)	γ^{AB}(mN/m)	γ^+ (mN/m)	γ^- (mN/m)	γ^{tot}(mN/m)
MC	38.4	4.6	1.1	5.1	43.1
ML	35.8	5.5	1.0	7.7	41.3
MM	34.5	5.4	1.1	7.1	39.9
MH	34.1	1	1.7	0.2	35.1
P. aeruginosa*	30.7	5.8	0.2	39.5	36.4
BSA*	26.7	0	0	39.5	26.7
Water*	21.8	51.0	25.5	25.5	72.8

*Data from literature [57–59]

3.3. Anti-adhesive and anti-microbial properties of nanocomposite membranes

The effect of the Al-NP interlayer in the attachment of foulants was evaluated experimentally by epifluorescence microscopy imaging of the different membranes after 3h of

contact time with *P. aeruginosa* cells or BSA. To image these foulants, bacterial cells were stained using Syto9 and PI, for live and dead staining, respectively, while the BSA protein used was a fluorescent FITC conjugate (Figure 6). For *P. aeruginosa* adhesion, compared to the control MC membrane where the number of bacterial cells was 7.3×10^4 cells/cm^2, the number of adhered cells was reduced on ML and MM to 5.1×10^4 and 4.9×10^4 cells/cm^2 (Figure 6A). On the other hand, MH shows remarkably higher number of bacteria adhered to the surface, with 20.1×10^4 cells/cm^2, or 275% of the control value. Similarly, BSA protein attachment, represented by the green florescence on the epifluorescence microscopy images (Figure 6B), was decreased for ML and MM membranes by 82% and 84% of the control value, while for MH there was an increase in BSA fluorescence on the membrane up to 649% of the control value. Therefore, both ML and MM membranes showed reduced fouling propensity while the higher Al-NPs loading, MH, drastically increased the deposition of both bacteria and proteins on the surface.

The surface properties of the different membranes were correlated with the deposition of *P. aeruginosa* cells using regression analyses to identify the most important changes in surface properties induced by Al-NPs that resulted in a decrease in bacterial deposition. The only surface properties that were significantly ($p<0.05$) correlated with bacterial deposition were ΔG_{sw} and WCA (Table S6). However, these two properties are intrinsically dependent on each other, with WCA being dependent on the ΔG_{sw}; therefore, only ΔG_{sw} was further considered. Adding surface roughness or density of carboxylic acid functional groups to ΔG_{sw} in a multiple regression analysis did not improve the statistical significance of the model and, consequently, ΔG_{sw} was found to be the main determinant for the change in bacterial deposition between the different membranes. This conclusion is in agreement with the findings of Grossman et al., who identified, using multiple regression analysis, that surface free energy was the most important parameter for biofouling on

ultrafiltration membranes [60]. Similarly, surface free energy was also identified as the most important determinant for biofouling on polypropylene spacers [12]. For BSA protein adsorption, while ΔG_{sw} still had the lowest *p* value in a single regression analysis, no surface properties were found to have a significant correlation ($p>0.05$ for all surface properties, Table S6) with BSA adsorption. This may suggest that other factors, such as foulant-foulant interactions [61], may have a more important role in the amount of protein adsorbing on the surface as compared to bacteria.

Live/dead staining of *P. aeruginosa* cells was also used to determine if the Al-NP interlayer imparted biocidal properties to the membrane. Based on fluorescence imaging of live and dead cells (Figure 6A), both ML and MM membranes showed lower cell attachment but higher viability compared to MC, increasing from 67% viability for cells attached to MC to 99% and 74% for cells on ML and MM, respectively. On the other hand, MH, which has the highest attachment, shows low cell viability (3%). This result could be the product of several interactions between membrane surface and bacteria cell. Direct contact between Al-NP, which may be emerging from the PA layer because of the large aggregates found in the MH membrane, and bacterial cells can lead to cell inactivation via membrane damage or oxidative stress,[62–65] even at low Al-NP concentration.[64,66] In addition, the accumulation of cells in regions highly prone to adhesion may stress the cells by reduction of mobility and locally increase cell inactivation [67]. Differential adhesion of live and dead cells on the different surfaces, or cell proliferation on non-biocidal membranes, may also explain the variation in cell viability observed for the different membranes. While the specific mechanisms of bacteria inactivation still need further studies, the current results show that the ML and MM membranes have lower bacterial deposition but low/no biocidal properties while the MH membrane has the highest bacterial deposition but lowest live cell density. While both mechanisms may slow down biofilm formation, dynamic biofouling experiments are

needed to establish which mechanisms, and type of membrane, achieve the highest biofouling resistance.

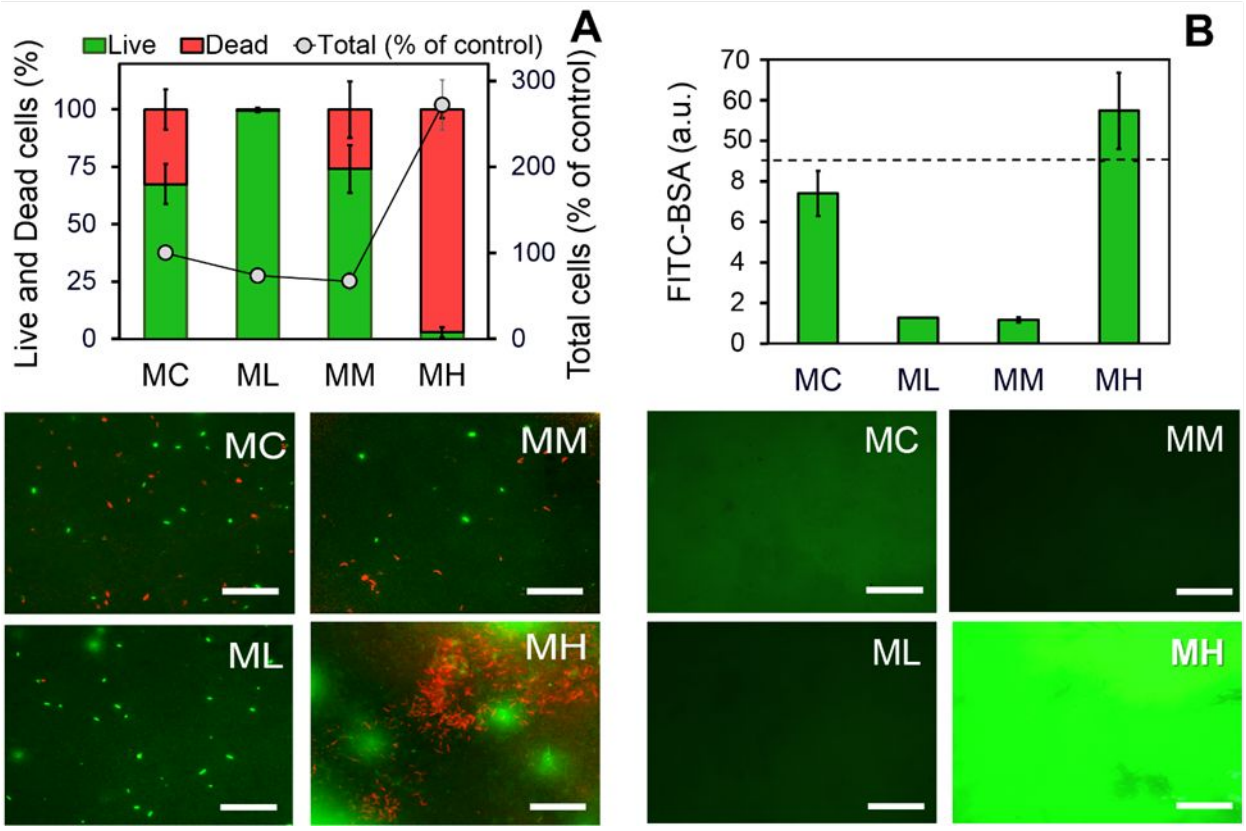

Figure 6. (A) Adhesion and viability of *P. aeruginosa* on membranes surface compared to control, counted by ImageJ of epifluorescence microscopy images (n=10) (scale bar: 50 µm). Live and dead cells are shown by green and red fluorescence, respectively. (B) Average of FITC-BSA fluorescence, quantified by ImageJ analysis of green pixels of epifluorescence microscopy images (n=10) (scale bar: 100 µm).

3.4. Dynamic biofouling

Although the static bacterial and protein deposition assays suggest promising fouling resistance, biofilm formation in membrane systems will also be influenced by the hydrodynamic conditions of the feed channel as well as the dynamics of the biofilm formation itself, which involve cell division and EPS production. Therefore, the biofouling propensity of the different membranes was evaluated under dynamic operating conditions using a bench-scale RO system. When operated with a synthetic secondary treated wastewater effluent supplemented with *P. aeruginosa* (2.5×10^8 cells/L) as feed water, all the membranes experienced flux decline over time due to the formation of biofilms on the surface (Figure 7A). After ~24h of operation, the permeate flux of membrane control declined by 51%, while, for the ML and MM membranes, the permeate flux experienced a lower decline of 37% and 26%, respectively (Figure 7B). Finally, the MH membranes, which had the highest deposition of bacteria and proteins in static conditions, also experienced the highest flux decline, with a 67% decrease in flux during the dynamic biofouling experiment. The higher flux decline for the MH membrane reveals that, for these Al-NP/PA membranes, the lower bacteria and protein deposition of ML and MM membranes is more important than the high cell inactivation, observed in MH, for biofouling resistance under dynamic conditions.

The biofilm structure on the ML and MM membranes was also significantly different, with only a thin and well-distributed biofilm layer compared to the mushroom-like structure biofilm on MC and MH membranes (Figure 7D). The uneven distribution of biofilm on MC surface may be related to the presence of larger PA peaks on the MC surface (Figure 2), which can act as shielding sites to entrap bacteria and protein [4]. Additionally, the magnitude of biofilm formation on the MH surface was unexpectedly lower compared to the discrepancy between the samples in static biofouling assays (Figure 7C). This result could be the consequence of several factors, which

include the presence of $CaCl_2$ in the synthetic wastewater used in these experiments. As discussed above, calcium is known to induce organic fouling by forming bridges between the carboxylic acid groups of both bacteria and PA [52]. The lower concentration of carboxylic groups in MH surface may have slowed down the initial attachment of *P. aeruginosa*. In addition, dead cells are known to be easily detached from the membrane surface by hydraulic rinsing [9]. Given the low viability of bacteria attachment on MH surface, the hydraulic rinsing may have favored the lower magnitude of biofilm formation compared to static biofouling assays.

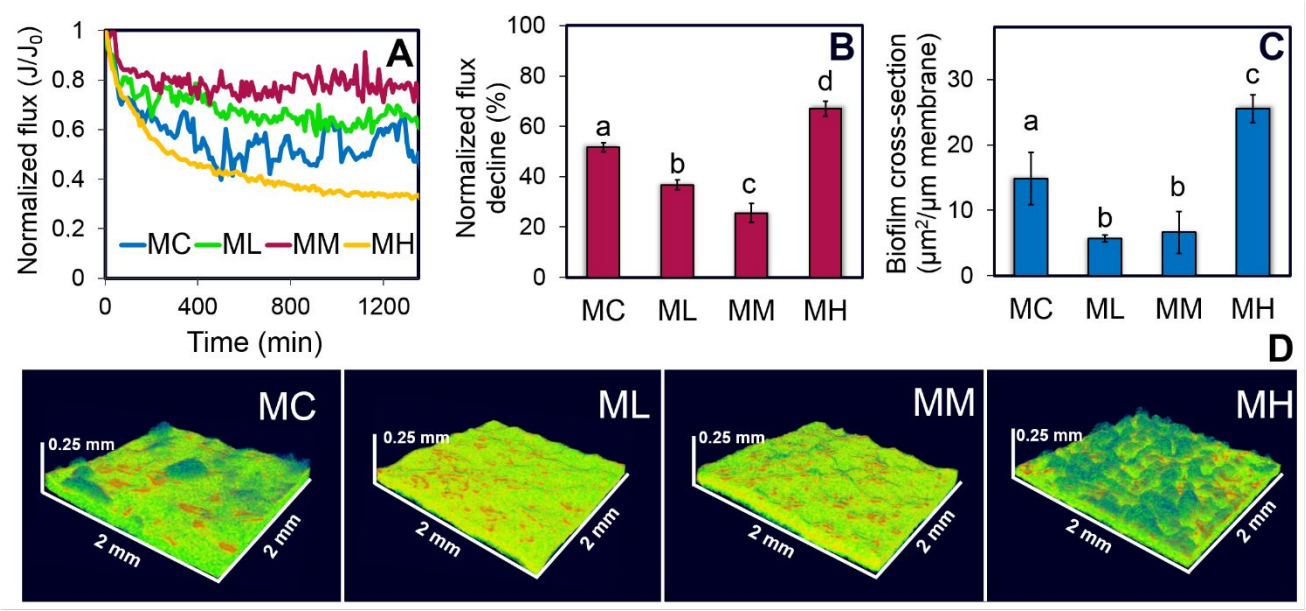

Figure 7. Normalized flux declines during (A) and after (B) 1350 min of biofilm formation. (C) Biofilm formation area (μm^2) cross-section of membranes (2 mm cuts), quantified by ImageJ, and (D) representative 3D optical coherence tomography imaging of the biofilm on membranes surface (2x2 mm cuts). Lower case letters indicate statistical significance (different letters representing statistical difference) (p-value <0.05), determined by One-way ANOVA (post hoc Tukey).

4. CONCLUSION

This study demonstrated that a nanoparticle-templated PA layer can improve the biofouling resistance of desalination membranes. The presence of an Al-NP interlayer results in changes in the PA formation that can increase the surface hydrophilicity and surface free energy of cohesion of the PA layer, which increase the energy barrier for the deposition of bacteria or proteins on the surface. However, to achieve high biofouling resistance, a good distribution of Al-NPs on the support structure is necessary. At high Al-NP loading on the support layer, the presence of agglomerates increased surface roughness and reduced the surface energy of cohesion, which increased membrane fouling. The use of an interlayer to guide the PA formation towards a less fouling-prone surface has several advantages compared to post-fabrication surface modifications since the antifouling character of the nanoparticle-templated membrane is a result of the intrinsic properties of the PA layer. In comparison, antifouling coatings externally applied to the membrane surface may wash off and be lost over time. Although further research on the optimal NP size, type, and loading is still needed to establish the use of nanoparticle interlayers as a strategy for fouling resistant membranes, the results of this study provide useful insights into the mechanisms involved in the antifouling properties of nanoparticle-templated PA layers to be used in desalination membrane fabrication.

ASSOCIATED CONTENT

Supporting information.

Silver method of carboxyl group quantification (S1). Determination of surface tension parameters (S2, Equation S1-S3, Table S1 and S2). Synthetic secondary wastewater recipe (Table S3). Support 3D AFM images (Figure S1). XPS detailed information (Table S4 and Figure S2).

Membrane performance (Figure S3). Carboxyl group reduction by quantitative method (Figure S4). Electrostatic double-layer adhesion energy and zeta potential (Table S5). Correlation between surface properties and *P. aeruginosa* cells or BSA protein adsorption (Table S6).

AUTHOR INFORMATION

Corresponding author

* Francois Perreault, Email: francois.perreault@asu.edu, Phone: (480) 965-4028

Funding Sources

N.M.J. received financial support from Coordenação de Aperfeiçoamento de Pessoal de Nível Superior (CAPES-Brazil). This work was funded by the Nanosystems Engineering Research Center for Nanotechnology-Enabled Water Treatment (EEC-1449500) and Conselho Nacional de Desenvolvimento Científico e Tecnológico (CNPq 473046/2013-0).

ACKNOWLEDGEMENT

We gratefully acknowledge the use of the characterization facilities within the LeRoy Eyring Center for Solid State Science at Arizona State University. The authors thank Dr. Eduardo A. Isoppo and Dr. Deise R. Consoli from LCME-UFSC for their support on the membrane cross-section preparation and FESEM analysis. The authors are grateful to MSc. Ana Barrios for her help with the XPS measurements. We also would like to thank Dr. Douglas Rice for his support on WCA and SFE analysis.

REFERENCES

1 M. A. Shannon, P. W. Bohn, M. Elimelech, J. G. Georgiadis, B. J. Mariñas, A. M. Mayes and A. M. Mayes, Science and technology for water purification in the coming decades, *Nature*, 2008, **452**, 337–346.

2 M. Qasim, M. Badrelzaman, N. N. Darwish, N. A. Darwish and N. Hilal, Reverse osmosis desalination: A state-of-the-art review, *Desalination*, 2019, **459**, 59–104.

3 H. C. Flemming, Biofouling and me: My Stockholm syndrome with biofilms, *Water Res.*, 2020, **173**, 115576.

4 P. S. Goh, A. K. Zulhairun, A. F. Ismail and N. Hilal, Contemporary antibiofouling modifications of reverse osmosis desalination membrane: A review, *Desalination*, 2019, **468**, 114072.

5 T. Yu, H. Sun, Z. Chen, Y. H. Wang, Z. Y. Huo, N. Ikuno, K. Ishii, Y. Jin, H. Y. Hu, Y. H. Wu and Y. Lu, Different bacterial species and their extracellular polymeric substances (EPSs) significantly affected reverse osmosis (RO) membrane fouling potentials in wastewater reclamation, *Sci. Total Environ.*, 2018, **644**, 486–493.

6 M. Herzberg and M. Elimelech, Biofouling of reverse osmosis membranes: Role of biofilm-enhanced osmotic pressure, *J. Memb. Sci.*, 2007, **295**, 11–20.

7 D. L. Zhao, S. Japip, Y. Zhang, M. Weber, C. Maletzko and T. S. Chung, *Water Res.*, 2020, 173, 115557.

8 S. F. Anis, R. Hashaikeh and N. Hilal, Reverse osmosis pretreatment technologies and future trends: A comprehensive review, *Desalination*, 2019, **452**, 159–195.

9 D. Saeki, H. Karkhanechi, H. Matsuura and H. Matsuyama, Effect of operating conditions on biofouling in reverse osmosis membrane processes: Bacterial adhesion, biofilm formation, and permeate flux decrease, *Desalination*, 2016, **378**, 74–79.

10 A. E. Contreras, Z. Steiner, J. Miao, R. Kasher and Q. Li, Studying the role of common membrane surface functionalities on adsorption and cleaning of organic foulants using QCM-D, *Environ. Sci. Technol.*, 2011, **45**, 6309–6315.

11 Y. Mo, A. Tiraferri, N. Y. Yip, A. Adout, X. Huang and M. Elimelech, Improved antifouling properties of polyamide nanofiltration membranes by reducing the density of surface carboxyl groups, *Environ. Sci. Technol.*, 2012, **46**, 13253–13261.

12 D. Rice, A. C. A. C. Barrios, Z. Xiao, A. Bogler, E. Bar-Zeev and F. Perreault, Development of anti-biofouling feed spacers to improve performance of reverse osmosis modules, *Water Res.*, 2018, **145**, 599–607.

13 S. Jiang, Y. Li and B. P. Ladewig, A review of reverse osmosis membrane fouling and control strategies, *Sci. Total Environ.*, 2017, **595**, 567–583.

14 G. Ye, J. Lee, F. Perreault and M. Elimelech, Controlled Architecture of Dual-Functional Block Copolymer Brushes on Thin-Film Composite Membranes for Integrated ‘defending’ and ‘attacking’ Strategies against Biofouling, *ACS Appl. Mater. Interfaces*, 2015, **7**, 23069–23079.

15 A. C. Barrios, D. Carrillo, T. R. Waag, D. Rice, Y. Bi, R. Islam and F. Perreault, *Prolonging the antibacterial activity of nanosilver-coated membranes through partial*

sulfidation, Royal Society of Chemistry, 2020, vol. 7.

16 J.-A.-D. Sharabati, S. Guclu, S. Erkoc-Ilter, D. Y. Koseoglu-Imer, S. Unal, Y. Z. Menceloglu, I. Ozturk and I. Koyuncu, Interfacially polymerized thin-film composite membranes: Impact of support layer pore size on active layer polymerization and seawater desalination performance, *Sep. Purif. Technol.*, 2019, **212**, 438–448.

17 J. R. Werber, C. O. Osuji and M. Elimelech, Materials for next-generation desalination and water purification membranes, *Nat. Rev. Mater.*, 2016, **1**, 16018.

18 C. Jiang, L. Tian, Z. Zhai, Y. Shen, W. Dong, M. He, Y. Hou and Q. J. Niu, Thin-film composite membranes with aqueous template-induced surface nanostructures for enhanced nanofiltration, *J. Memb. Sci.*, 2019, **589**, 117244.

19 Y. Liang, Y. Zhu, C. Liu, K. Lee, W. Hung, Z. Wang, Y. Li, M. Elimelech, J. Jin and S. Lin, Polyamide nanofiltration membrane with highly uniform sub-nanometre pores for sub-1 Å precision separation, *Nat. Commun.*, 2020, **11**, 1–9.

20 Z. Wang, Z. Wang, S. Lin, H. Jin, S. Gao, Y. Zhu and J. Jin, Nanoparticle-templated nanofiltration membranes for ultrahigh performance desalination, *Nat. Commun.*, , DOI:10.1038/s41467-018-04467-3.

21 G. Z. Ramon, M. C. Y. Wong and E. M. V. Hoek, Transport through composite membrane, Part 1: Is there an optimal support membrane?, *J. Memb. Sci.*, 2012, **415–416**, 298–305.

22 A. K. Ghosh and E. M. V. Hoek, Impacts of support membrane structure and chemistry on polyamide-polysulfone interfacial composite membranes, *J. Memb. Sci.*, 2009, **336**, 140–148.

23 S. Al Aani, A. Haroutounian, C. J. Wright and N. Hilal, Thin Film Nanocomposite (TFN) membranes modified with polydopamine coated metals/carbon-nanostructures for desalination applications, *Desalination*, 2018, **427**, 60–74.

24 M. B. Wu, Y. Lv, H. C. Yang, L. F. Liu, X. Zhang and Z. K. Xu, Thin film composite membranes combining carbon nanotube intermediate layer and microfiltration support for high nanofiltration performances, *J. Memb. Sci.*, 2016, **515**, 238–244.

25 Z. Yang, H. Guo, Z. K. Yao, Y. Mei and C. Y. Tang, Hydrophilic Silver Nanoparticles Induce Selective Nanochannels in Thin Film Nanocomposite Polyamide Membranes, *Environ. Sci. Technol.*, 2019, **53**, 5301–5308.

26 J. J. Wang, H. C. Yang, M. B. Wu, X. Zhang and Z. K. Xu, Nanofiltration membranes with cellulose nanocrystals as an interlayer for unprecedented performance, *J. Mater. Chem. A*, 2017, **5**, 16289–16295.

27 Y. Zhu, W. Xie, S. Gao, F. Zhang, W. Zhang, Z. Liu and J. Jin, Single-Walled Carbon Nanotube Film Supported Nanofiltration Membrane with a Nearly 10 nm Thick Polyamide Selective Layer for High-Flux and High-Rejection Desalination, *Small*, 2016, **12**, 5034–5041.

28 X. Wang, S. Cong and J. Ma, A biomimetic strategy for improving activity of nano zero-valent iron based on the adhesive behavior of polydopamine on PVDF·Al2O3film, *Mater. Chem. Phys.*, 2017, **197**, 215–225.

29 D. Chen, J. R. Werber, X. Zhao and M. Elimelech, A facile method to quantify the carboxyl group areal density in the active layer of polyamide thin-film composite membranes, *J. Memb. Sci.*, 2017, **534**, 100–108.

30 S. Azari, L. Zou and E. Cornelissen, Assessing the effect of surface modification of polyamide RO membrane by l-DOPA on the short range physiochemical interactions with biopolymer fouling on the membrane, *Colloids Surfaces B Biointerfaces*, 2014, **120**, 222–228.

31 D. Song, W. Zhang, W. Cheng, B. Jia, P. Wang, Z. Sun, J. Ma, X. Zhai, J. Qi and C. Liu, Micro fine particles deposition on gravity-driven ultrafiltration membrane to modify the surface properties and biofilm compositions: Water quality improvement and biofouling mitigation, *Chem. Eng. J.*, , DOI:10.1016/j.cej.2019.123270.

32 R. X. Zhang, L. Braeken, P. Luis, X. L. Wang and B. Van der Bruggen, Novel binding procedure of TiO2 nanoparticles to thin film composite membranes via self-polymerized polydopamine, *J. Memb. Sci.*, 2013, **437**, 179–188.

33 Z. Yang, Y. Wu, J. Wang, B. Cao and C. Y. Tang, In situ reduction of silver by polydopamine: A novel antimicrobial modification of a thin-film composite polyamide membrane, *Environ. Sci. Technol.*, 2016, **50**, 9543–9550.

34 J. Zhu, A. Uliana, J. Wang, S. Yuan, J. Li, M. Tian, K. Simoens, A. Volodin, J. Lin, K. Bernaerts, Y. Zhang and B. Van Der Bruggen, Elevated salt transport of antimicrobial loose nanofiltration membranes enabled by copper nanoparticles: Via fast bioinspired deposition, *J. Mater. Chem. A*, 2016, **4**, 13211–13222.

35 F. J. Sikora and M. B. McBride, Aluminum Complexation by Catechol as Determined by Ultraviolet Spectrophotometry, *Environ. Sci. Technol.*, 1989, **23**, 349–356.

36 R. Subair, B. P. Tripathi, P. Formanek, F. Simon, P. Uhlmann and M. Stamm, Polydopamine modified membranes with in situ synthesized gold nanoparticles for

catalytic and environmental applications, *Chem. Eng. J.*, 2016, **295**, 358–369.

37 X. Ma, Z. Yang, Z. Yao, H. Guo, Z. Xu and C. Y. Tang, Tuning roughness features of thin film composite polyamide membranes for simultaneously enhanced permeability, selectivity and anti-fouling performance, *J. Colloid Interface Sci.*, 2019, **540**, 382–388.

38 D. Emadzadeh, W. J. Lau, T. Matsuura, M. Rahbari-Sisakht and A. F. Ismail, A novel thin film composite forward osmosis membrane prepared from PSf–TiO2 nanocomposite substrate for water desalination, *Chem. Eng. J.*, 2014, **237**, 70–80.

39 L. Huang, S. Zhao, Z. Wang, J. Wu, J. Wang and S. Wang, In situ immobilization of silver nanoparticles for improving permeability, antifouling and anti-bacterial properties of ultrafiltration membrane, *J. Memb. Sci.*, 2016, **499**, 269–281.

40 M. R. Mehrnia, Y. M. Mojtahedi and M. Homayoonfal, What is the concentration threshold of nanoparticles within the membrane structure? A case study of Al2O3/PSf nanocomposite membrane, *Desalination*, 2015, **372**, 75–88.

41 M. Sianipar, S. H. Kim, C. Min, L. D. Tijing and H. K. Shon, Potential and performance of a polydopamine-coated multiwalled carbon nanotube/polysulfone nanocomposite membrane for ultrafiltration application, *J. Ind. Eng. Chem.*, 2016, **34**, 364–373.

42 Y. Baek, H. J. Kim, S. H. Kim, J. C. Lee and J. Yoon, Evaluation of carbon nanotube-polyamide thin-film nanocomposite reverse osmosis membrane: Surface properties, performance characteristics and fouling behavior, *J. Ind. Eng. Chem.*, 2017, **56**, 327–334.

43 Z. Yang, F. Wang, H. Guo, L. E. Peng, X. H. Ma, X. X. Song, Z. Wang and C. Y. Tang, Mechanistic Insights into the Role of Polydopamine Interlayer toward Improved Separation Performance of Polyamide Nanofiltration Membranes, *Environ. Sci. Technol.*,

2020, **54**, 11611–11621.

44 M. Wu, J. Yuan, H. Wu, Y. Su, H. Yang, X. You, R. Zhang, X. He, N. A. Khan, R. Kasher and Z. Jiang, Ultrathin nanofiltration membrane with polydopamine-covalent organic framework interlayer for enhanced permeability and structural stability, *J. Memb. Sci.*, 2019, **576**, 131–141.

45 R. Dai, J. Li and Z. Wang, Constructing interlayer to tailor structure and performance of thin-film composite polyamide membranes: A review, *Adv. Colloid Interface Sci.*, 2020, **282**, 102204.

46 Y. H. Kotp, High-flux TFN nanofiltration membranes incorporated with Camphor-Al2O3 nanoparticles for brackish water desalination, *Chemosphere*, 2021, **265**, 128999.

47 J. Yin, G. Zhu and B. Deng, Graphene oxide (GO) enhanced polyamide (PA) thin-film nanocomposite (TFN) membrane for water purification, *Desalination*, 2016, **379**, 93–101.

48 A. P. Rao, S. V. Joshi, J. J. Trivedi, C. V. Devmurari and V. J. Shah, Structure-performance correlation of polyamide thin film composite membranes: Effect of coating conditions on film formation, *J. Memb. Sci.*, 2003, **211**, 13–24.

49 H. Zhao, S. Qiu, L. Wu, L. Zhang, H. Chen and C. Gao, Improving the performance of polyamide reverse osmosis membrane by incorporation of modified multi-walled carbon nanotubes, *J. Memb. Sci.*, 2014, **450**, 249–256.

50 B. Rajaeian, A. Rahimpour, M. O. Tade and S. Liu, Fabrication and characterization of polyamide thin film nanocomposite (TFN) nanofiltration membrane impregnated with TiO2 nanoparticles, *Desalination*, 2013, **313**, 176–188.

51 Y. Mo, K. Xiao, Y. Shen and X. Huang, A new perspective on the effect of complexation

between calcium and alginate on fouling during nanofiltration, *Sep. Purif. Technol.*, 2011, **82**, 121–127.

52 M. Xie, E. Bar-Zeev, S. M. Hashmi, L. D. Nghiem and M. Elimelech, Role of Reverse Divalent Cation Diffusion in Forward Osmosis Biofouling, *Environ. Sci. Technol.*, 2015, **49**, 13222–13229.

53 J. A. Brant and A. E. Childress, Colloidal adhesion to hydrophilic membrane surfaces, *J. Memb. Sci.*, 2004, **241**, 235–248.

54 Y. Li, C. Li, S. Li, B. Su, L. Han and B. Mandal, Graphene oxide (GO)-interlayered thin-film nanocomposite (TFN) membranes with high solvent resistance for organic solvent nanofiltration (OSN), *J. Mater. Chem. A*, 2019, **7**, 13315–13330.

55 M. Safarpour, A. Khataee and V. Vatanpour, Thin film nanocomposite reverse osmosis membrane modified by reduced graphene oxide/TiO2 with improved desalination performance, *J. Memb. Sci.*, 2015, **489**, 43–54.

56 R. Pang, J. Li, K. Wei, X. Sun, J. Shen, W. Han and L. Wang, In situ preparation of Al-containing PVDF ultrafiltration membrane via sol-gel process, *J. Colloid Interface Sci.*, 2011, **364**, 373–378.

57 C. J. van Oss, Acid-base interfacial interactions in aqueous media, *Colloids Surfaces A Physicochem. Eng. Asp.*, 1993, **78**, 1–49.

58 S. Kim and E. M. V. Hoek, Interactions controlling biopolymer fouling of reverse osmosis membranes, *Desalination*, 2007, **202**, 333–342.

59 D. Grasso, B. F. Smets, K. A. Strevett, B. D. Machinist, C. J. Van Oss, R. F. Giese and W. Wu, Impact of physiological state on surface thermodynamics and adhesion of

Pseudomonas aeruginosa, *Environ. Sci. Technol.*, 1996, **30**, 3604–3608.

60 A. D. Grossman, Y. Yang, U. Yogev, D. C. Camarena, G. Oron and R. Bernstein, Effect of ultrafiltration membrane material on fouling dynamics in a submerged anaerobic membrane bioreactor treating domestic wastewater, *Environ. Sci. Water Res. Technol.*, 2019, **5**, 1145–1156.

61 B. Ma, G. Wu, W. Li, R. Miao, X. Li and P. Wang, Roles of membrane–foulant and inter/intrafoulant species interaction forces in combined fouling of an ultrafiltration membrane, *Sci. Total Environ.*, 2019, **652**, 19–26.

62 M. A. Ansari, H. M. Khan, A. A. Khan, S. S. Cameotra, Q. Saquib and J. Musarrat, Interaction of Al2O3 nanoparticles with Escherichia coli and their cell envelope biomolecules, *J. Appl. Microbiol.*, 2014, **116**, 772–783.

63 S. Parham, D. H. B. Wicaksono, S. Bagherbaigi, S. L. Lee and H. Nur, Antimicrobial Treatment of Different Metal Oxide Nanoparticles: A Critical Review, *J. Chinese Chem. Soc.*, 2016, **63**, 385–393.

64 M. Bhuvaneshwari, S. Bairoliya, A. Parashar, N. Chandrasekaran and A. Mukherjee, Differential toxicity of Al2O3 particles on Gram-positive and Gram-negative sediment bacterial isolates from freshwater, *Environ. Sci. Pollut. Res.*, 2016, **23**, 12095–12106.

65 S. Pakrashi, D. Kumar, V. Iswarya, M. Bhuvaneshwari, N. Chandrasekaran and A. Mukherjee, A comparative ecotoxicity analysis of α- and γ-phase aluminium oxide nanoparticles towards a freshwater bacterial isolate Bacillus licheniformis, *Bioprocess Biosyst. Eng.*, 2014, **37**, 2415–2423.

66 S. Pakrashi, S. Dalai, D. Sabat, S. Singh, N. Chandrasekaran and A. Mukherjee,

Cytotoxicity of Al 2O 3 nanoparticles at low exposure levels to a freshwater bacterial isolate, *Chem. Res. Toxicol.*, 2011, **24**, 1899–1904.

67 Y. R. Chang, E. R. Weeks and W. A. Ducker, Surface Topography Hinders Bacterial Surface Motility, *ACS Appl. Mater. Interfaces*, 2018, **10**, 9225–9234.